SUPPLEMENTARY INFORMATION

ADDITIONAL AND SUPPLEMENTARY METHODS

DNA constructs

EGFP-tagged human β-actin was purchased from Clontech (Mountain View, CA, USA). Photoactivatable GFP (PA-GFP) was kindly provided by George Patterson and Jennifer Lippincott-Schwartz (Patterson and Lippincott-Schwartz, 2002). For cofilin expression, murine cofilin and human EGFP-cofilin (Mannherz et al., 2005) were cloned into pGEX-6P-1 (GE Healthcare). The fidelity of all constructs was verified by sequencing. All other constructs were as described: PA-GFP-actin (Koestler et al., 2008), photoactivatable mRFP-actin (Pacholsky et al., 2004), EGFP-ArpC5B (Rottner et al., 2006), EGFP-Abi-1 (Innocenti et al., 2005), EGFP-WAVE2 (Benesch et al., 2002), EGFP-VASP (Carl et al., 1999), EGFP-CP-beta2 (Schafer et al., 1998), EGFP-cortactin constructs (Kaksonen et al., 2000; van Rossum et al., 2003; Zhu et al., 2007), EGFP-tagged wildtype and active (S3A) as well as inactive (S3D) cofilin (Mannherz et al., 2005).

Immunoprecipitation

The immunoprecipitation experiment shown in Supplementary Figure 8 was performed using protein A-sepharose (SIGMA, Munich, Germany) according to standard protocols, except that actin in lysates was loaded with ADP for 30 minutes, to take advantage of the increased binding affinity of ADP-actin to cofilin (Yeoh et al., 2002). B16-F1 cells were transfected with EGFP-tagged wildtype cofilin or the S3A- or S3D-mutant, and tagged

proteins precipitated using monoclonal anti-GFP antibodies (BD Biosciences, Heidelberg, Germany). Supernatants and precipitated proteins were probed with polyclonal anti-actin antibodies (anti-actin C11; SIGMA, Munich; Germany). Peroxidase-labelled secondary antibodies were from Cell Signalling (Danvers, Mass, USA).

Video microscopy and TIRF

Time-lapse microscopy using epi-fluorescence and phase contrast optics as shown in Supplementary Figures 1 and 5 were done on an inverted Axiovert S100TV (Zeiss, Jena, Germany) essentially as described (Steffen et al., 2004) using a 100x 1.4 plan-apochromatic objective with 1.6 optovar intermediate magnification. Tungsten lamps and heat-filters were used for both transmitted and epi-fluorescence illumination. The experiment shown in Supplementary Figure 6 was done on an inverted Axiovert 200 (Zeiss, Jena, Germany) equipped with a 100W mercury lamp and an EM-CCD camera (Cascade II, Photometrics, USA). Latrunculin B was from SIGMA (Munich, Germany).

TIRF microscopy used in Supplementary Figure 8 was performed essentially as described before (Kovar and Pollard, 2004), with the exception that rabbit skeletal actin was labelled at Cys-374 with Alexa-488 C_5-maleimide. All experiments were performed with proteins mixed in "TIRF-polymerisation-buffer" (10mM imidazole pH 7.4, 50mM KCl, 1mM $MgCl_2$, 1mM EGTA, 0.2mM ATP, 50mM DTT, 15mM glucose, 20µg/ml catalase, 100µg/ml glucose oxidase, and 0.5% methylcellulose (4000 cP)), and examined in custom-made glass slide chambers.

Data analysis and presentation

FRAP data were analysed essentially as described (Rabut and Ellenberg, 2005). Best linear fits were calculated using SigmaPlot 10.0 (Scientific Solutions SA, Pully-Lausanne, Switzerland). For treadmilling analysis, the lamellipodium was divided into front and back halves and the respective intensities measured over time (as indicated in Figure 1F). Background fluorescence intensities taken from a region outside the cell (see Supplementary Information, Movie 5) were subtracted from each individual region and frame. Acquisition photobleaching was subtracted as recommended (Rabut and Ellenberg, 2005) and determined using a stable cellular region (usually cytosolic) largely unaffected by experimental bleaching. The average fluorescence intensity as obtained from the lamellipodial regions flanking both sides of the bleached area upon fluorescence recovery was defined as maximum and normalized to 1. For components residing at lamellipodial tips, half time of fluorescence recovery ($t_{1/2}$) was determined only, whereas proteins localizing to the entire lamellipodium were in addition subjected to treadmilling analysis. Best linear fits for tip components, front- and rear-half as well as entire-lamellipodium (not shown) recovery curves corresponded to the following equation: $y = a(1-\exp(-bx))$, except for data obtained from rear-half recovery measurements of actin and Arp2/3-complex, which best fitted to sigmoid curves corresponding to equation: $y = y_0 + a/(1 + \exp(-(x-x_0)/b))$. $t_{1/2}$ values were calculated by solving the corresponding equations with a fluorescence intensity of 50% of the maximum recovery value.

For determining treadmilling factors (TMF), normalized intensities of front- and rear-half lamellipodial regions were plotted over time. The TMF for a given component, expressed in arbitrary units (a.u.), was defined as the average difference in fluorescence recovery

between front and back half of the lamellipodium (per second recovery time), and thus calculated as follows: Area under intensity curve for the rear (∫B) was subtracted from that for the front (∫F), and divided by the time (in seconds) required for 100% recovery (Figure 1F).

Simulation of actin recovery in the lamellipodium

Modelling is exemplified in detail for the model shown in Figure 1D. Diffusion and retrograde transport of actin were modelled in a 2-dimensional matrix 200 simulation cells (SCs) long and 400 SCs wide representing a region of the leading lamella 40 μm long along the leading edge and extending 20 μm backwards from the leading edge. Thus each SC was 0.2 μm long and 0.05 μm wide. The simulation was initialised by a uniform random distribution of 10,000,000 molecules of G-actin and 10,000,000 molecules of F-actin throughout the matrix. This gives a mean density of total actin of 25,000 molecules/μm^2 which, assuming a lamellipodial thickness of 0.1μm, corresponds to a micromolarity of 415 in the lamellipodium. The exact concentration of actin chosen is unimportant as it only affects the noise in the images of the model.

Simulation was carried out in Mathematica version 5.2. At the beginning of each second of real time, any F-actin remaining in the rearmost row of the matrix (of which there is almost none in the steady state) is first converted into G-actin. The whole array of F-actin is then moved bodily backwards by 1 SC. This corresponds to a retrograde transport of F-actin of 0.05 μm/s or 3μm/min, which is within the range of values for real cells and quite a close match to the particular cell being modelled (Figure 1A). The remainder of the 1-second interval is occupied by four simulation cycles of G/F-actin transitions and G-actin

diffusion. The G-to-F (polymerisation) transitions and F-to-G (depolymerisation) transitions during each 0.25 second-interval are chosen at random for each molecule using the probability functions shown in Figure 1E. Finally, there are 68 diffusion steps of 0.2μm along each axis during each simulation cycle. Thus, during a single diffusion step, each G-actin molecule moves at random 1 SC in either direction sideways and 4 SCs forward or backward with reflection at boundaries in each case. This corresponds to a diffusion coefficient of $0.5 \times 4 \times 68 \times 0.22 = 5.44\ \mu m^2/s$, which is close to the value determined experimentally for G-actin diffusing in cytoplasm (McGrath et al., 1998). The state of the model is displayed as an actin density image at the end of each 1-second interval.

Before simulation of bleaching, the model was run for about 2 min to allow it to settle down to a steady state. In the steady state, the region of high density F-actin extended 3-4μm back from the leading edge, which corresponds well with average lamellipodial dimensions of real cells. Importantly, the transition probability functions of Figure 1E were chosen by trial and error to obtain the best match. Bleaching was simulated by removing all actin molecules from the model in a square region of approximately 14 × 14 μm with one edge situated centrally on the leading edge. The model was then run for a further minute of real time to observe the redistribution of labelled actin after bleaching. To keep the model as simple and robust as possible, no attempts were made to simulate the forward protrusion of the leading edge or the F-actin density gradient in the lamellipodium.

For obtaining models with variable lamellipodium widths used for the analyses shown in Supplementary Figure 2b, the same parameters were used except for that the depolymerisation probability profiles (dpp) were changed as shown in Supplementary Figure 2a. This generated models with a range of widths, which were subsequently bleached as described above. For treadmilling analyses, the measured areas in all models were selected to reflect lamellipodia with equal fluorescence intensity gradients, with an average intensity decay of 80% for the back half as compared to the front half of the lamellipodium. As a result, the lamellipodial widths analysed corresponded to 5µm, 3.5µm, 2.1µm, 1.6µm and 0.7µm for models dpp1 - dpp5, respectively. Treadmilling factors obtained were plotted versus lamellipodium width, and curved-fitted (Supplementary Figure 2b).

SUPPLEMENTARY FIGURE LEGENDS

Supplementary Figure 1 Arp2/3-complex localizes to the entire lamellipodium. Epi-fluorescence (top) and phase contrast (bottom) images derived from a time-lapse movie of a B16-F1 cell transiently expressing EGFP-ArpC5B (p16). Double-headed arrows highlight the width of the lamellipodium as observed in phase contrast, which is mirrored by EGFP-ArpC5B accumulation in epi-fluorescence. Time is in seconds; bar = 5µm.

Supplementary Figure 2a Steady state results of lamellipodial simulation with F → G actin probability profiles as displayed in the top left panel, called depolymerisation

profile (dpp) 1 – 5. Blue and red curves depict F-actin and G-actin intensity profiles as a function of distance from the leading edge for all five conditions as indicated.

Supplementary Figure 2b The treadmilling factor (TMF) is sensitive to lamellipodium width. Lamellipodium width plotted *versus* TMFs measured from actin FRAP simulations shown in Supplementary Figure 2a.

Supplementary Figure 3 VASP turnover at the lamellipodium is comparably slow. (**A**) FRAP of the Ena/VASP family member VASP at the lamellipodium tip. Bar: 2µm. (**B**) Average fluorescence recovery of EGFP-VASP at the lamellipodium tip plotted over time. Data are means and SEMs of 5 independent movies. $t_{1/2}$ of fluorescence recovery was calculated using best linear fit (green).

Supplementary Figure 4 FRAP recovery dynamics of alternative EGFP-cortactin constructs. (**A**) FRAP of EGFP-cortactin (construct 2, cortactin cloned into EGFP-N1, Clontech) (Kaksonen et al., 2000) as indicated (see also Supplementary Movie 12). Time is in seconds; bar = 5µm. (**B**) Treadmilling analysis of EGFP-cortactin construct 2. Plotted are averaged data (means and SEMs of means) and best linear fits of 5 independent movies. $t_{1/2}$ given was calculated for entire lamellipodium. Although half time of fluorescence recovery was accelerated as compared to construct 1 (Figure 3A), the TMFs obtained for both constructs were virtually identical, corroborating the conclusion of homogenous recovery of cortactin throughout the lamellipodium. (**C**) Representative FRAP experiment of B16-F1 cell expressing another EGFP-cortactin

construct (construct 3, (Zhu et al., 2007). Note again homogenous recovery throughout the lamellipodium. Time is in seconds; bar = 5μm.

Supplementary Figure 5 Capping protein is restricted to the lamellipodium front. Epi-fluorescence (top) and phase contrast (bottom) images from a time-lapse movie of a B16-F1 cell expressing EGFP-tagged CP-beta2 (CP). Double headed arrows mark the width of the lamellipodium as observed in phase contrast. Note that the localization of capping protein is largely confined to the tip region of the lamellipodium. Time is in seconds, bar = 5μm.

Supplementary Figure 6 Latrunculin B treatment abolishes capping protein localisation at the lamellipodium front. Epi-fluorescence (Epi) and phase contrast (Phase) images from a time-lapse movie of a B16-F1 cell expressing EGFP-tagged CP-beta2 (CP) treated with 5μM Latrunculin B (LatB) (added at time 0). Arrows mark EGFP-tagged CP-beta2 at the lamellipodium front. Time is in seconds, bar = 5μm.

Supplementary Figure 7 Precipitation of cofilin-ADP-actin complexes from cell lysates. Western blot showing actin staining (arrow) of supernatants (lanes 1-3) and protein A-sepharose pellets (lanes 5-7) after immunoprecipitation with anti-GFP antibodies of extracts from cells expressing EGFP-tagged cofilin wildtype (lanes 1, 5), cofilin-S3A (lanes 2, 6) or cofilin-S3D (lanes 3, 7). Transfection efficiency was equal in all samples as confirmed by Western Blotting (not shown). Lane 4 was loaded with purified rabbit skeletal muscle actin (1 μg) as control. All EGFP-tagged cofilin variants are capable of

actin binding in cell extracts, albeit with less efficiency in the case of the inactive mutant (S3D, lane 7).

Supplementary Figure 8 Fragmentation of individual actin filaments by untagged and EGFP-cofilin. Time lapse micrographs of the spontaneous polymerisation of a mixture of unlabelled actin (1μM) and Alexa-Fluor-488 actin (0.3μM) alone (top), in the presence of 200nM untagged cofilin (middle) or 200nM EGFP-cofilin (bottom). Arrows indicate individual cutting events. Both cofilin and EGFP-cofilin display severing on growing actin filaments. Time is in seconds, bar = 5μm.

SUPPLEMENTARY REFERENCES

Benesch, S., Lommel, S., Steffen, A., Stradal, T.E., Scaplehorn, N., Way, M., Wehland, J. and Rottner, K. (2002) Phosphatidylinositol 4,5-biphosphate (PIP2)-induced vesicle movement depends on N-WASP and involves Nck, WIP, and Grb2. *J Biol Chem*, **277**, 37771-37776.

Carl, U.D., Pollmann, M., Orr, E., Gertlere, F.B., Chakraborty, T. and Wehland, J. (1999) Aromatic and basic residues within the EVH1 domain of VASP specify its interaction with proline-rich ligands. *Curr Biol*, **9**, 715-718.

Innocenti, M., Gerboth, S., Rottner, K., Lai, F.P., Hertzog, M., Stradal, T.E., Frittoli, E., Didry, D., Polo, S., Disanza, A., Benesch, S., Di Fiore, P.P., Carlier, M.F. and Scita, G. (2005) Abi1 regulates the activity of N-WASP and WAVE in distinct actin-based processes. *Nat Cell Biol*, **7**, 969-976.

Kaksonen, M., Peng, H.B. and Rauvala, H. (2000) Association of cortactin with dynamic actin in lamellipodia and on endosomal vesicles. *J Cell Sci*, **113 Pt 24**, 4421-4426.

Koestler, S.A., Auinger, S., Vinzenz, M., Rottner, K. and Small, J.V. (2008) Differentially oriented populations of actin filaments generated in lamellipodia collaborate in pushing and pausing at the cell front. *Nat Cell Biol*, **in press**.

Kovar, D.R. and Pollard, T.D. (2004) Insertional assembly of actin filament barbed ends in association with formins produces piconewton forces. *Proc Natl Acad Sci U S A*, **101**, 14725-14730.

Mannherz, H.G., Gonsior, S.M., Gremm, D., Wu, X., Pope, B.J. and Weeds, A.G. (2005) Activated cofilin colocalises with Arp2/3 complex in apoptotic blebs during programmed cell death. *Eur J Cell Biol*, **84**, 503-515.

Pacholsky, D., Vakeel, P., Himmel, M., Lowe, T., Stradal, T., Rottner, K., Furst, D.O. and van der Ven, P.F. (2004) Xin repeats define a novel actin-binding motif. *J Cell Sci*, **117**, 5257-5268.

Patterson, G.H. and Lippincott-Schwartz, J. (2002) A photoactivatable GFP for selective photolabeling of proteins and cells. *Science*, **297**, 1873-1877.

Rabut, G. and Ellenberg, J. (2005) Photobleaching Techniques to Study Mobility and Molecular Dynamics of Proteins in Live Cells: FRAP, iFRAP, and FLIP. In Goldman, R.D. and Spector, D.L. (eds.), *Live Cell Imaging, A Laboratory Manual*. Cold Spring Harbor Laboratory Press, New York, pp. 101-126.

Rottner, K., Kaverina, I.N. and Stradal, T.E.B. (2006) Cytoskeleton Proteins. In Celis, J.E. (ed.), *Cell Biology, A Laboratory Handbook*. Elsevier Acadmic Press, London, Vol. 3, pp. 111-119.

Schafer, D.A., Welch, M.D., Machesky, L.M., Bridgman, P.C., Meyer, S.M. and Cooper, J.A. (1998) Visualization and molecular analysis of actin assembly in living cells. *J Cell Biol*, **143**, 1919-1930.

Steffen, A., Rottner, K., Ehinger, J., Innocenti, M., Scita, G., Wehland, J. and Stradal, T.E. (2004) Sra-1 and Nap1 link Rac to actin assembly driving lamellipodia formation. *Embo J*, **23**, 749-759.

van Rossum, A.G., de Graaf, J.H., Schuuring-Scholtes, E., Kluin, P.M., Fan, Y.X., Zhan, X., Moolenaar, W.H. and Schuuring, E. (2003) Alternative splicing of the actin binding domain of human cortactin affects cell migration. *J Biol Chem*, **278**, 45672-45679.

Yeoh, S., Pope, B., Mannherz, H.G. and Weeds, A. (2002) Determining the differences in actin binding by human ADF and cofilin. *J Mol Biol*, **315**, 911-925.

Zhu, J., Yu, D., Zeng, X.C., Zhou, K. and Zhan, X. (2007) Receptor-mediated endocytosis involves tyrosine phosphorylation of cortactin. *J Biol Chem*, **282**, 16086-16094.

Supplementary Figure 1

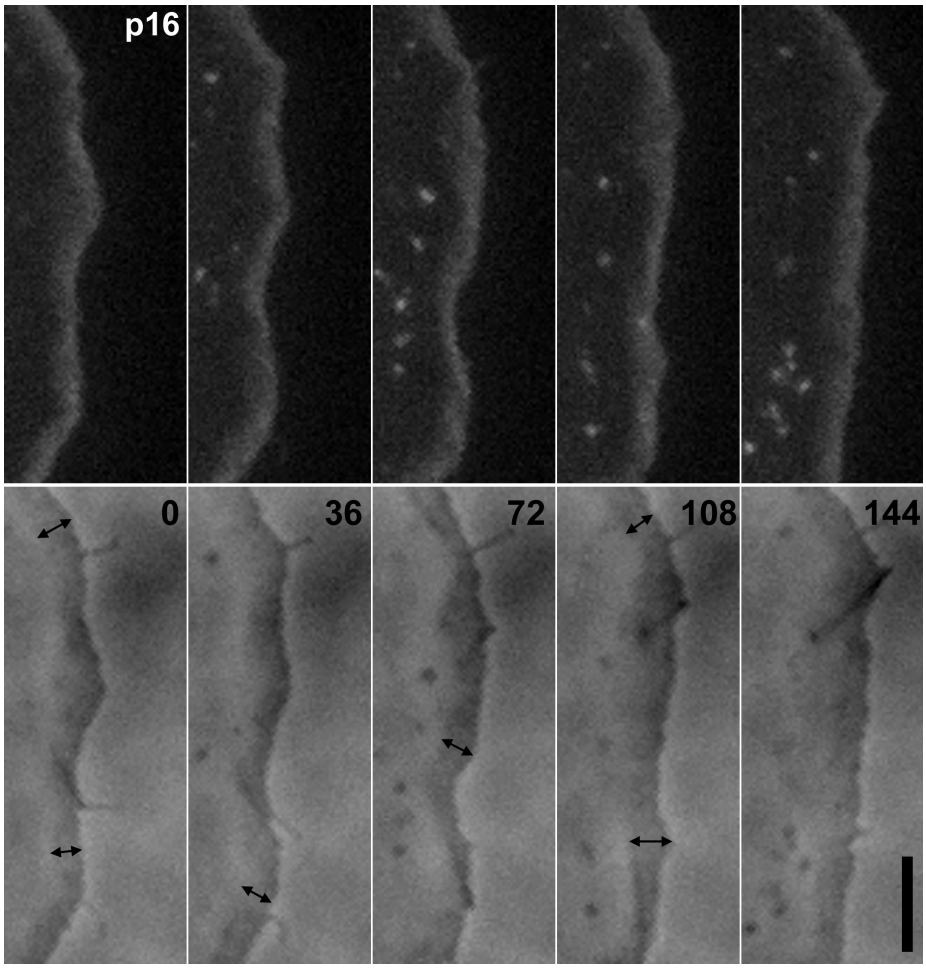

Supplementary Figure 2a

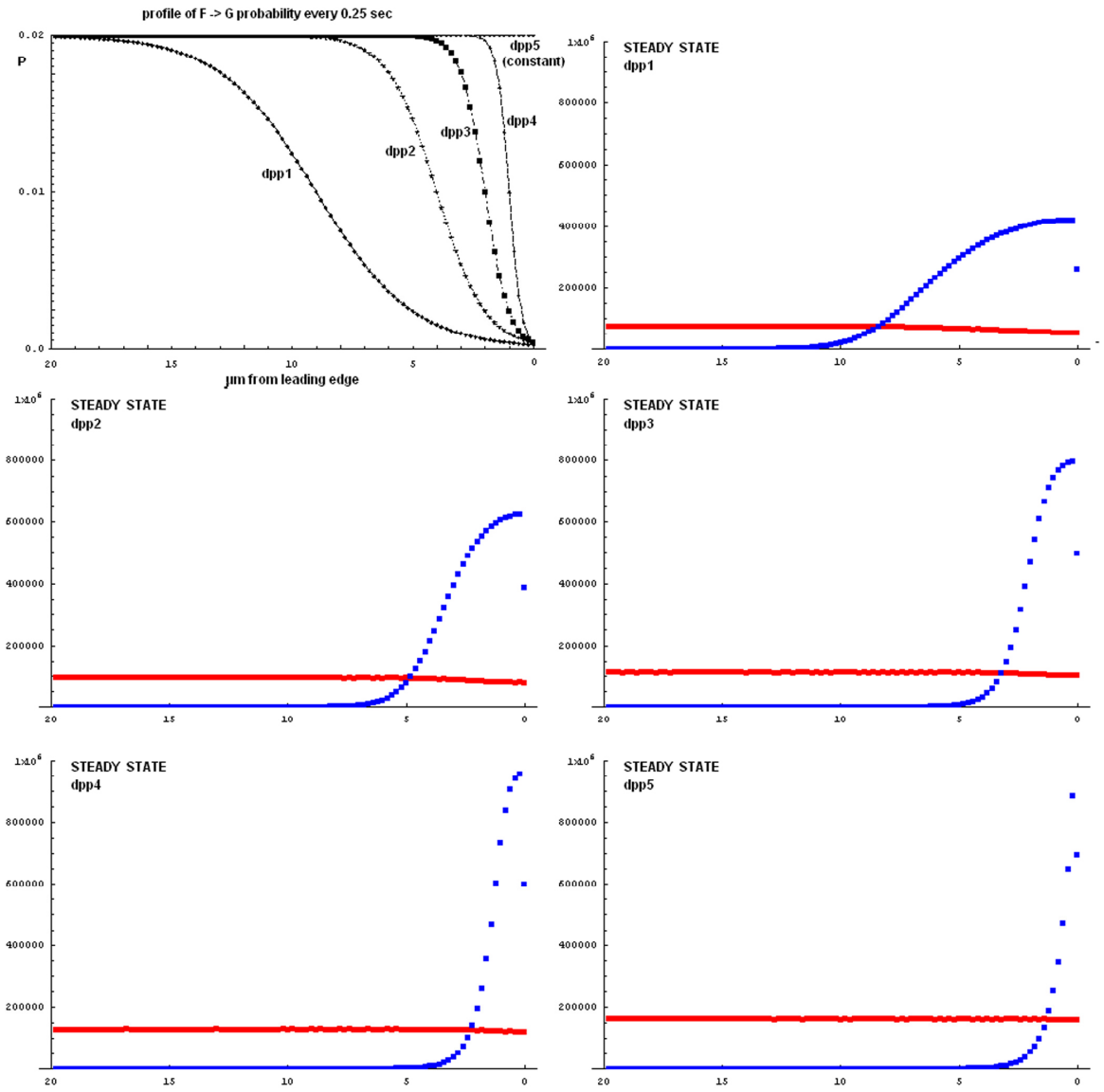

Supplementary Figure 2b

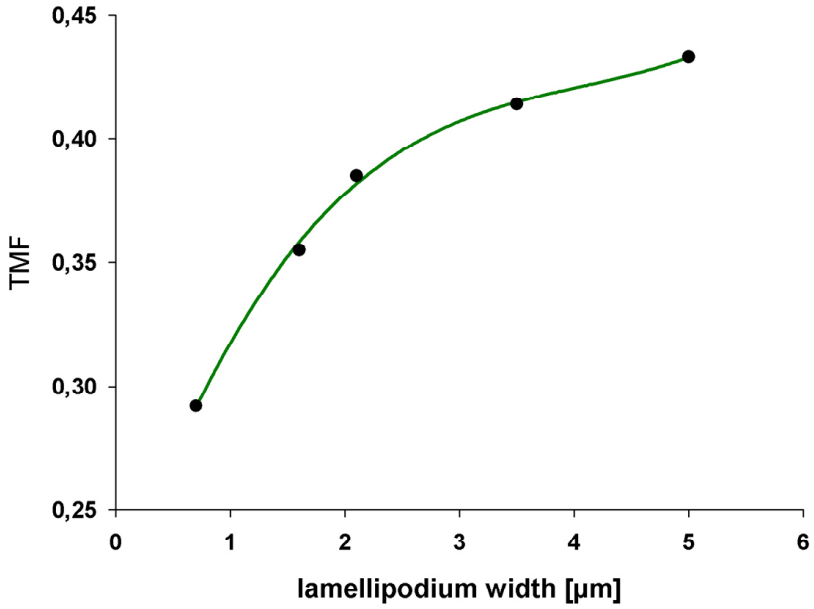

Supplementary Figure 3

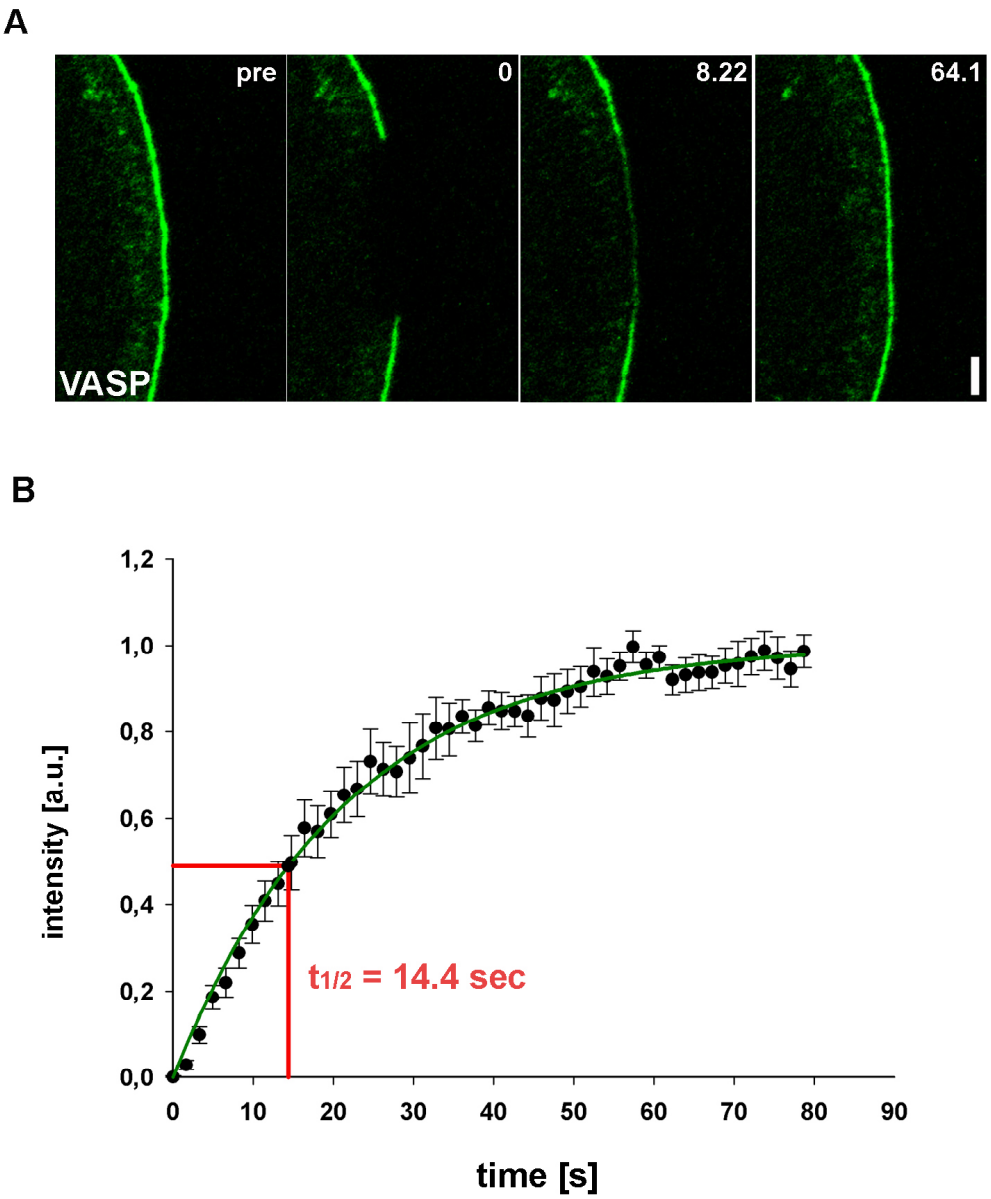

Supplementary Figure 4

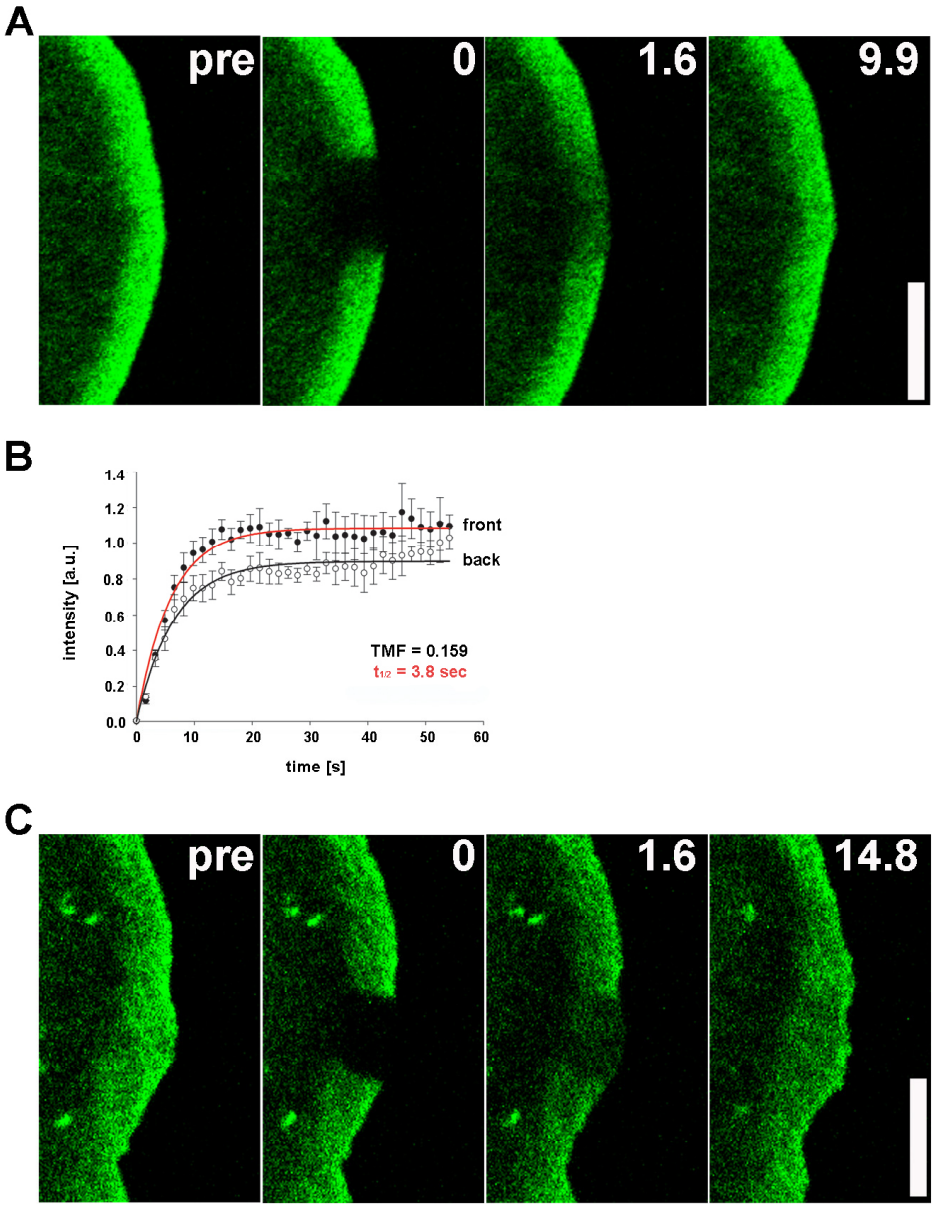

Supplementary Figure 5

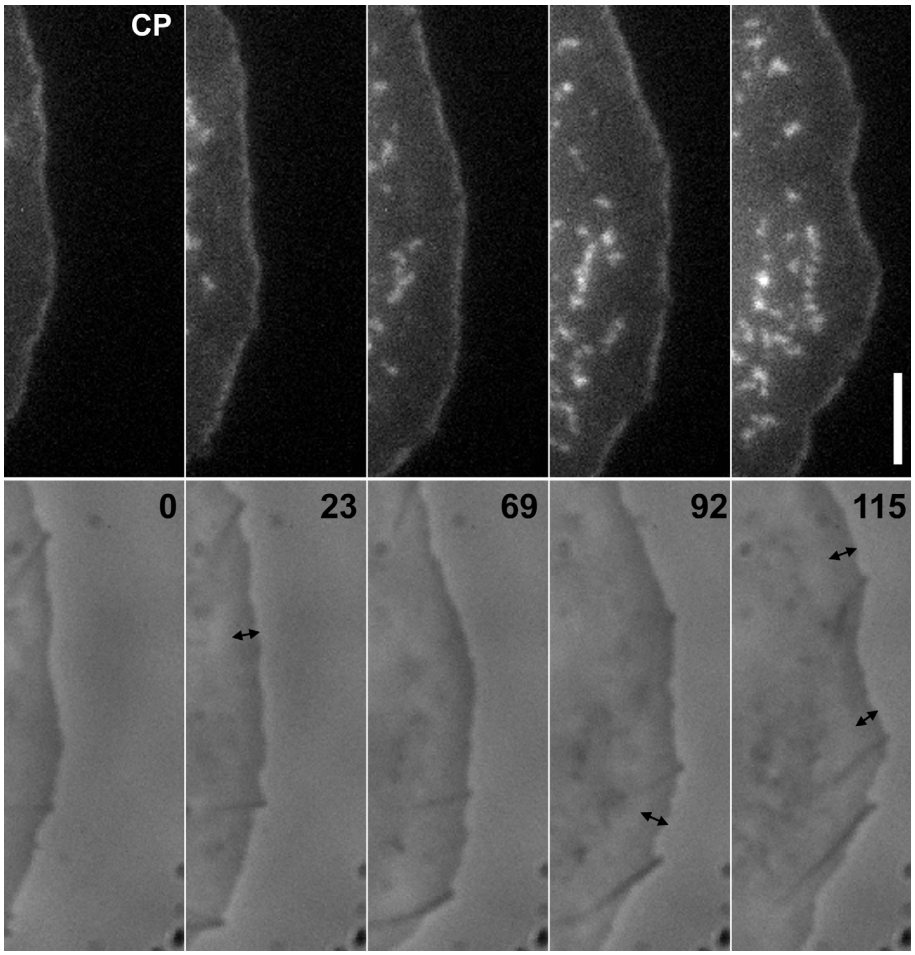

Supplementary Figure 6

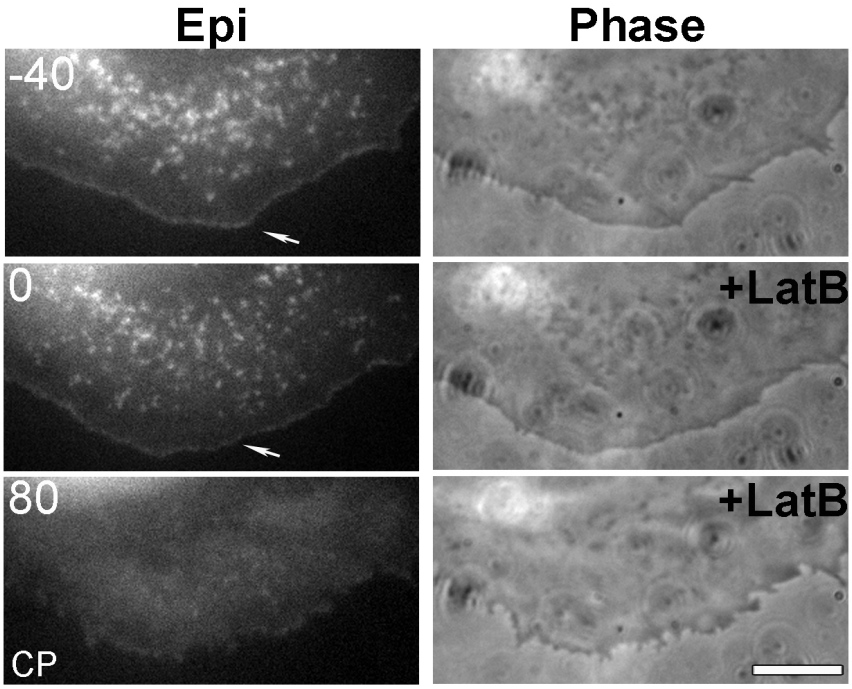

Supplementary Figure 7

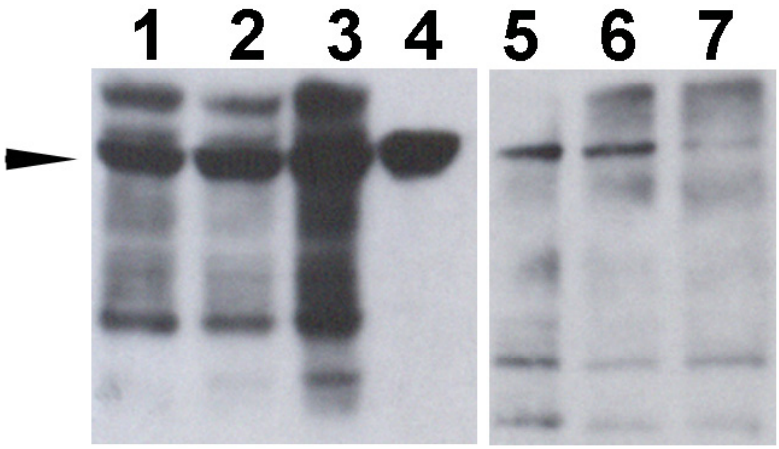

Supplementary Figure 8